AGU PUBLICATIONS

JGR

Journal of Geophysical Research: Atmospheres

RESEARCH ARTICLE
10.1002/2016JD025965

Key Points:
- MJO modulates radiative fields with near-zero net-tropospheric cooling during its active phase due to longwave absorption and re-emission
- Radiative heating rates exhibit tilted structures with height reflecting changes in the cloud population and associated water vapor fields
- Over the MJO lifecycle net-tropospheric radiation varies ~0.5 K/d enhancing the amplitude of the convective heating signal by ~20%

Correspondence to:
P. E. Ciesielski,
paulc@atmos.colostate.edu

Citation:
Ciesielski, P. E., R. H. Johnson, X. Jiang, Y. Zhang, and S. Xie (2017), Relationships between radiation, clouds, and convection during DYNAMO, *J. Geophys. Res. Atmos.*, *122*, 2529–2548, doi:10.1002/2016JD025965.

Received 19 SEP 2016
Accepted 13 FEB 2017
Accepted article online 16 FEB 2017
Published online 1 MAR 2017

Relationships between radiation, clouds, and convection during DYNAMO

Paul E. Ciesielski[1], Richard H. Johnson[1], Xianan Jiang[2], Yunyan Zhang[3], and Shaocheng Xie[3]

[1]Department of Atmospheric Science, Colorado State University, Fort Collins, Colorado, USA, [2]Joint Institute for Regional Earth System Science and Engineering, University of California, Los Angeles, California, USA, [3]Lawrence Livermore National Laboratory, Livermore, California, USA

Abstract The relationships between radiation, clouds, and convection on an intraseasonal time scale are examined with data taken during the Dynamics of the Madden-Julian Oscillation (MJO) field campaign. Specifically, column-net, as well as vertical profiles of radiative heating rates, computed over Gan Island in the central Indian Ocean (IO) are used along with an objective analysis of large-scale fields to examine three MJO events that occurred during the 3 month period (October to December 2011) over this region. Longwave (LW) and shortwave radiative heating rates exhibit tilted structures, reflecting radiative effects associated with the prevalence of shallow cumulus during the dry, suppressed MJO phase followed by increasing deep convection leading into the active phase. As the convection builds going into the MJO active phase, there are increasingly top-heavy anomalous radiative heating rates while the column-net radiative cooling rate $<Q_r>$ progressively decreases. Temporal fluctuations in the cloud radiative forcing, being quite sensitive to changes in high cloudiness, are dominated by LW effects with an intraseasonal variation of ~0.4–0.6 K/d. While both the water vapor and cloud fields are inextricably linked, it appears that the tilted radiative structures are more related to water vapor effects. The intraseasonal variation of column-net radiative heating $<Q_r>$ enhances the convective signal in the mean by ~20% with a minimum in this enhancement ~10 days prior to peak MJO rainfall and maximum ~7 days after. This suggests that as MJO convective envelope weakens over the central IO, cloud-radiative feedbacks help maintain the mature MJO as it moves eastward.

1. Introduction

The Madden-Julian Oscillation (MJO) [*Madden and Julian*, 1972] dominates tropical intraseasonal variability, and its impact beyond the tropics on both global weather and climate is profound [*Zhang*, 2013]. Due to its intraseasonal nature and broad global impacts, the MJO can serve as a key element for seamless weather prediction, bridging the gap between deterministic weather forecasts and climate prediction. For this goal to be realized the deficiencies in our understanding of the MJO's essential physics, as evidenced by poor MJO simulations in many current general circulation models (GCMs), must be resolved [*Petch et al*., 2011; *Hung et al*., 2013; *DeMott et al*., 2015]. Motivated to improve understanding, model performance, and forecasts of the MJO, the climate community has dedicated significant effort to investigating the key physical processes responsible for the MJO's initiation and propagation [*Jiang et al*., 2015; *Zhang et al*., 2013].

Previous studies have demonstrated that diabatic heating (including both convective and radiative effects) plays a crucial role in MJOs [e.g., *Yanai et al*., 2000; *Lin et al*., 2004; *Jiang et al*., 2011; *Lappen and Schumacher*, 2014]. This heating induces a large-scale circulation [e.g., *Schubert and Masarik*, 2006; *Wang and Liu*, 2011], which in turn feeds back on convection [e.g., *Kerns and Chen*, 2014], air-sea interaction [e.g., *Emanuel*, 1987; *Flatau et al*., 1997], and radiative processes [e.g., *Hu and Randall*, 1994; *Kim et al*., 2015] resulting in a complex, multiscale phenomenon in which an envelope of convective clouds propagates slowly eastward along the equator. Over the past several decades field campaign and reanalysis data sets have been used to examine the intraseasonal variability of diabatic heating Q_1 with an emphasis on the component connected to convective processes, which includes latent heat release and divergence of eddy heat fluxes [*Johnson and Ciesielski*, 2000; *Kiladis et al*., 2005]. Only in more recent years have emerging MJO model studies demonstrated that radiative effects can impact various aspects of simulated MJOs [e.g., *Raymond*, 2001; *Lee et al*., 2001; *Bony and Emanuel*, 2015; *Kim et al*., 2011; *Andersen and Kuang*, 2012; *Arnold et al*., 2013; *Crueger and Stevens*, 2015; *Wolding et al*., 2016]. These studies showed that when radiative heating reaches a critical fraction of convective heating (~20%) radiative-convective instability could result in MJO-like modes [*Yu et al*., 1998].

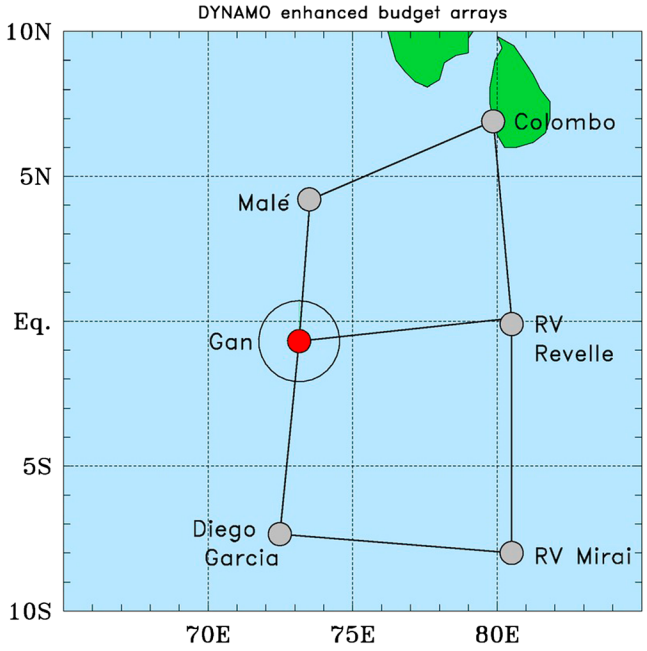

Figure 1. Map showing the DYNAMO enhanced sounding network. Observations for this study are focused on the Gan Island site (red circle) at 0.69°S, 73.15°E. The outer circle around Gan indicates domain for AMIE-Gan large-scale objective analyses used in this study.

Following up on this notion, *Lin and Mapes* [2004, hereafter LM04] used a variety of data sets over the tropical western Pacific to show that the column-integrated radiative heating is nearly in phase with the MJO rainfall peak and enhances preexisting convective heating by 10–15%. Though falling short of the critical 20% ratio, LM04 speculated that ratios could be much larger over western Indian Ocean (IO). By way of contrast, after examining output from several GCMs, *Jiang et al*. [2015] noted a negative correlation between model MJO amplitude and the strength of radiative feedback across these multimodel simulations. Thus, the impact of radiative effects on the MJO remains a matter of debate.

Radiative effects on convective self-aggregation have also been extensively investigated in recent studies [e.g., *Wing and Emanuel*, 2014; *Holloway and Woolnough*, 2016; *Coppin and Bony*, 2015], which may also have implications for the instability mechanism of the MJO [e.g., *Arnold and Randall*, 2015]. Despite the lack of consensus, different roles of LW and SW radiation, as well as surface fluxes, are suggested during different stages of convection organization.

To investigate the mechanisms responsible for the initiation of the MJO over the IO, the Dynamics of the MJO (DYNAMO) experiment was conducted during the period from October 2011 to March 2012 [*Yoneyama et al*., 2013]. A significant component of the experiment involved an enhanced network of upper air sounding sites over the central IO (Figure 1) composed of two quadrilateral arrays—one north and one south of the equator—referred to as the northern and southern sounding arrays or NSA and SSA. During the special observing period of the experiment (1 October to 30 November 2011) these sites took four to eight sounding observations per day. A supersite located at Gan Island (0.69°S, 73.2°E), part of the Atmospheric Radiation Measurement Program (ARM) MJO Investigation Experiment (AMIE), had multiple radars, radiometers, and conducted eight per day sounding operations through 8 February 2012. The sounding and radar observations were quality-controlled and bias-corrected, as needed, as part of special effort to produce high-quality research data sets [*Ciesielski et al*., 2014; *Xu et al*., 2015]. Based on the Gan cloud radar and other observations, a high-vertical and temporal resolution radiative heating rate product was produced for the DYNAMO period [*Feng et al*., 2014].

Leveraging upon these unprecedented observations, in particular those taken on Gan Island, this paper investigates the relationships between radiation, clouds, and convection on an intraseasonal time scale during DYNAMO to provide a clearer picture of the radiative impacts on the MJO. This study builds upon the recent analyses of *Ma and Kuang* [2011], *Del Genio and Chen* [2015, hereafter DC15], and *Kim et al*. [2017], who used data sets processed from NASA's A-Train constellation to examine cloud-radiative effects on the MJO and the boreal summer intraseasonal oscillation. Our results will demonstrate that the Gan radiative analyses, derived from ground-based instrumentation, compare quite well with the 10-MJO composite of DC15 based on 5 years of A-Train twice-daily radiative retrievals over the equatorial warm pool region.

The analyses herein will also provide some unique diagnostic metrics to evaluate GCMs and potentially expose reasons for their good and bad MJO simulations. These metrics include convective and radiative vertical profiles as a function of rain rate, composite convective and radiative fields relative to MJO peak

rainfall, and quantification of cloud and water vapor radiative effects during MJO passage. Finally, we will revisit the radiative-convective instability analyses previously examined for the DYNAMO NSA [*Sobel et al*., 2014; *Johnson et al*., 2015] with data sets collected from the Gan region.

2. Data and Procedure

SW and LW broadband fluxes and radiative heating profiles are obtained from the Pacific Northwest National Laboratory (PNNL) Combined Retrieval (CombRet) product based on cloud profiles, provided primarily by a zenith-pointing Doppler Ka-band cloud radar (KAZR) merged with S-band dual polarization Doppler radar observations, and sounding-based thermodynamic measurements at Gan Island [*Feng et al*., 2014], which were input to a delta-four-stream correlated *k*-distribution radiative transfer model [*Mather et al*., 2007; *Fu and Liou*, 1992]. The product used in this study is at 1 h, 25 hPa resolution (from 1000 to 50 hPa) for the period from 10 October 2011 to 08 February 2012. The version of CombRet data used in this study was produced by replacing the observed 2 m temperature with the sea surface temperature in the near vicinity of Gan, which makes the radiative fields more representative of open ocean conditions. Radiative fields are available for both all-sky and clear-sky conditions allowing us to estimate cloud radiative forcing (CRF) effects. These data were averaged into 3 h bins to match the temporal resolution of rainfall data. As an important point of caution, it is noted that high-level clouds (i.e., cirrus) were underestimated by radars on Gan Island due to signal attenuation and insufficient radar sensitivity, which will impact the radiative estimates as shown later.

Large-scale fields, including apparent heating Q_1 and drying Q_2, were obtained from the AMIE-Gan objective analyses patterned after the procedure of *Xie et al*. [2004]. These analyses, representative of a near circular region with a 150 km radius centered on Gan, were available at 3 h resolution for the period from 2 October to 31 December 2011 when the overall DYNAMO observational network was most complete [*Ciesielski et al*., 2014] and MJO activity was well established [*Gottschalck et al*., 2013]. The AMIE-Gan analyses were constructed by using the variational analysis method [*Zhang and Lin*, 1997; *Zhang et al*., 2001] in which atmospheric fields are constrained with observed surface and top of the atmosphere measurements with surface rainfall being the strongest constraint. Here the analyses were constrained by the C-band Shared Mobile Atmospheric Research Teaching Radar (SMART-R) rainfall estimates which were derived by using the Z-R relationship, $Z = 178\ R^{1.44}$, developed from the Mirai Indian Ocean cruise the Study of MJO onset (MISMO) field campaign. Additional details of how the SMART-R rainfall product was produced are given in *DePasquale et al*. [2014]. The estimated uncertainty in 3 h domain-averaged SMART-R rainfall increases with rain rate but is generally $<10\%$ (Weixin Xu 2016, personal communication). As noted in *DePasquale et al*. [2014], beam blockage at low levels resulted in the SMART-R products being processed only in a 180° sector between 338° and 158°. To address the uncertainty from SMART-R's partial coverage of the domain, the SMART-R rainfall ($P_{\text{SMART-R}}$) was adjusted as follows:

$$P_{\text{SMART-R adjusted}} = P_{\text{SMART-R}} * P_{\text{TRMM\_150km\_domain}} / P_{\text{TRMM\_SMART-R\_domain}} \quad (1)$$

This adjustment retains the variability of the Tropical Rainfall Measuring Mission (TRMM) 3B42 rainfall but with the magnitude set by the SMART-R. The use of the surface rainfall constraint in the analyses ensures that the vertically integrated large-scale heat and moisture budgets are consistent with the observed precipitation over the region.

In the absence of a sounding network on the scale of the radar coverage around Gan, the atmospheric state for the AMIE-Gan analyses was defined by sampling the operational European Centre for Medium-Range Weather Forecasts (ECMWF) analyses at eight grid points in circle with a 150 km radius around Gan Island, i.e., the area over which radar rainfall maps were available.

The approach of constraining a background atmospheric state based on model analyses, as opposed to actual sounding observations, is described in *Xie et al*. [2004]. Confidence for using the ECMWF analyses as a realistic background field comes from the fact that it assimilated observations from the enhanced DYNAMO sounding network (Figure 1). A comparison of sounding data to ECMWF analyses [*Johnson and Ciesielski*, 2013] showed excellent agreement in the basic fields. The primary exception to this is from 100

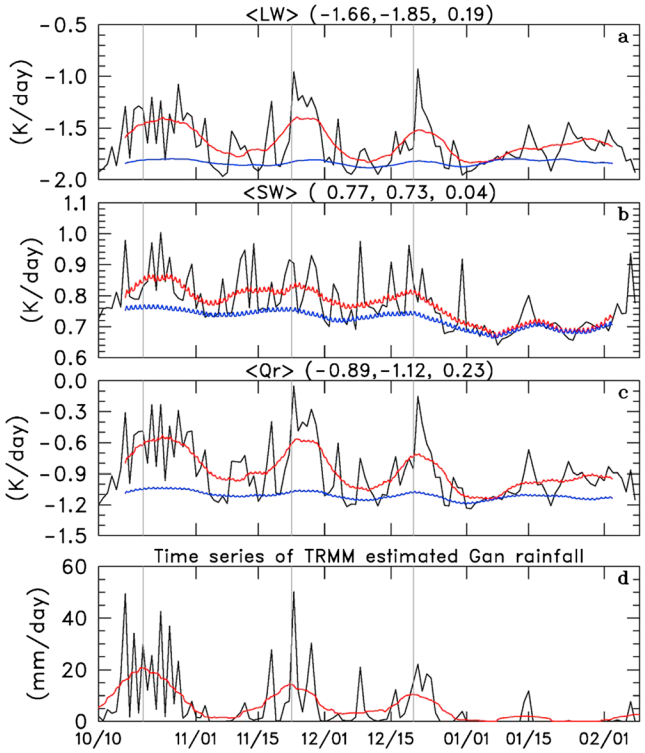

Figure 2. Time series of CombRet (a) <LW>, (b) <SW>, (c) $<Q_r>$, and (d) TRMM-estimated Gan rainfall where the black lines are daily-averaged values, while the red (blue) lines are LP-filtered values using 3 h all-sky (clear-sky) data. Numbers in parentheses represent the time mean all-sky, clear-sky, and CRF conditions, respectively. LP-filtered rainfall peaks for each MJO are indicated by thin vertical lines.

and 250 hPa where a 20% relative humidity (RH) difference is found between ECMWF analyses and sounding data, with ECMWF being moister [*Ciesielski et al.*, 2014].

Other data used in this study include fractional cloudiness and column-averaged radiation estimates (both all-sky and clear-sky) provided by the Clouds and the Earth's Radiant Energy System (CERES) product at 3 h resolution on a 1° grid [*Wielicki et al.*, 1996]. Computed CERES fluxes are produced by using the Langley Fu-Liou radiative transfer model [*Fu and Liou*, 1992]. Computations use Moderate Resolution Imaging Spectroradiometer and geostationary satellite cloud properties along with atmospheric properties provided by NASA's Modern-Era Retrospective analysis for Research and Applications (MERRA) [*Rienecker et al.*, 2011]. *Wielicki et al.* [1996] states that the science requirement for errors in the CERES top-of-atmosphere daily net flux is 5–10 W/m^2. However, high-level thin cirrus clouds, the effects of which were captured in DC15 by their use of A-Train cloud products that combine lidar and radar detection from space, would be underestimated in the CERES product. Rainfall data were from the TRMM 3B42 V7 product at 0.25°, 3 h resolution [*Huffman et al.*, 2007]. Stratiform rain fraction (SRF) data are based on the SMART-R radar retrievals using the convective-stratiform classification described in *Xu et al.* [2015]. The CERES, TRMM rainfall, and SRF data were averaged over a 150 km radius centered at Gan Island.

For the results to be shown, we define the column-integrated diabatic heating following *Yanai and Johnson* [1993] as

$$\begin{aligned} < Q_1 > &= LP_o + S + < Q_r > \\ &= < Q_{\text{conv}} > + < Q_r > \end{aligned} \tag{2}$$

where

$$<> = 1/g \int_{p_{\text{TOP}}}^{p_s} () \, dp$$

is the vertical integral from the top pressure level p_{TOP} (taken here to be 70 hPa) to the surface pressure p_S, Q_1 is the diabatic heating, Q_{conv} is the convective heating, S is the surface sensible heat flux, P_o is the surface precipitation, L is the latent heat of vaporization, and Q_r is the net (shortwave + longwave or SW + LW) radiative heating rate.

To focus on intraseasonal aspects of these fields, all data were subjected to a low-pass (LP) filter in time to retain variability at frequencies 20 days and longer. For this purpose a Kaiser symmetric filter [*Hamming*, 1989] with 48 terms was employed, which means that 6 days of 3 h data (or 48 data points) are lost at the ends of the time series.

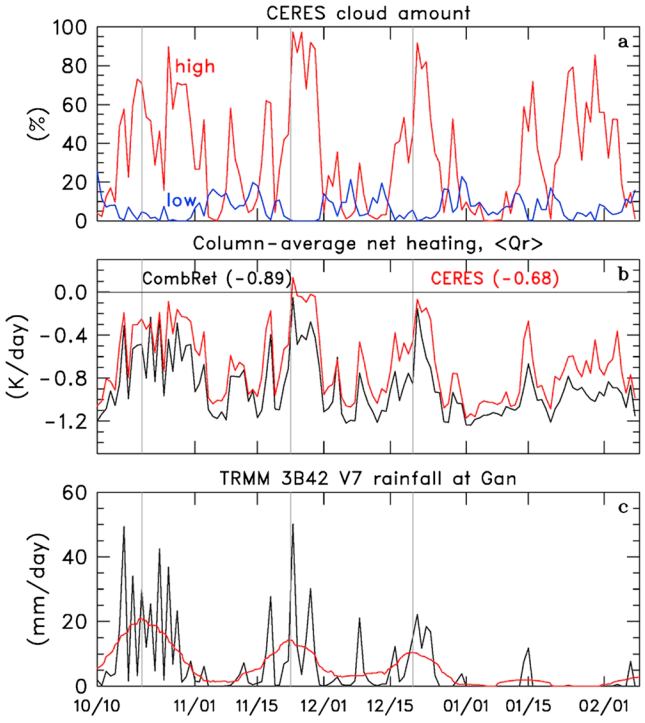

Figure 3. Time series of (a) daily-averaged CERES cloud amount for high clouds (red) and low clouds (blue); (b) column-average net heating $<Q_r>$ from CombRet product (black) and CERES (red), time mean is given in parentheses; and (c) Gan rainfall (black and red lines as in Figure 2). CERES values represent an average in a circle with a 150 km radius centered at Gan. LP-filtered rainfall peaks for each MJO are indicated by thin vertical lines.

3. Results

3.1. Intraseasonal Variation of Radiation, Clouds, and Rainfall

The time series of the CombRet column-averaged radiative fields and TRMM rainfall for the period of interest are shown in Figure 2. During this period three MJO events propagated through this region with convectively active periods, as evidenced in low-pass-filtered Gan rainfall, peaking in mid-October, late-November, and late-December. Rainfall was suppressed in January 2012. Associated with this rainfall modulation, all-sky <LW> and $<Q_r>$ cooling are reduced during the rainy periods, while all-sky <SW> heating increases slightly. The largest all-sky net cooling $<Q_r>$ occurs during the January suppressed period. We also note a prominent 2 day signal in all daily-averaged fields (black lines) associated with the October MJO. The small oscillations (~0.02 K/d) in the <SW> curves in Figures 2b and 4b are related to leakage of the diurnal signal (~2.5 K/d) due to using a filter with a finite number of terms.

Since radiative profiles are impacted by both water vapor and clouds, CRF effects are isolated by examining the difference between the all-sky and clear-sky radiative heating rates (i.e., CRF = all-sky − clear-sky; $<Q_r>_{CRF}$ = difference between red and blue lines in Figure 2). The amplitude of the clear-sky intraseasonal variation is about 10% of the all-sky amplitude such that CRF effects dominate any significant intraseasonal variations seen in the all-sky radiative fields. Also noteworthy in these time series, is the fact that the variations in the $<Q_r>_{CRF}$ are dominated by LW effects over SW with an intraseasonal amplitude in the CombRet product of about 0.4 K/d. Corresponding analyses based on CERES data (not shown) are generally similar except that the intraseasonal amplitudes of the CERES CRF <LW> and $<Q_r>$ are larger (i.e., ~0.5 K/d) consistent with the analyses shown later in Figure 4.

The evolution of cloudiness in the vicinity of Gan during the period of interest is shown in Figure 3 along with a comparison to rainfall and to all-sky $<Q_r>$ from the CombRet and CERES data sets. In comparing these two radiative products, one should bear in mind that some differences may be attributed to localized effects in the CombRet point measurements that are not present in the area-averaged CERES values. The strong anticorrelation between high (300–100 hPa) and low (surface to 700 hPa) cloud amounts seen here and in Figure 4d is at least partly a result of the blocking of low clouds by higher-level clouds. The sensitivity of $<Q_r>$ to high cloudiness is readily apparent with decreased cooling rates during periods of abundant high clouds, confirming the importance of high-level clouds in absorbing and re-emitting LW radiation in the troposphere [e.g., *Hartmann et al.*, 1992; *Stephens et al.*, 1994]. In fact, during the MJO active periods the column-net cooling rate is reduced to near zero with even slight warming seen during the November MJO. The 0.21 K/d negative offset in the CombRet $<Q_r>$ product relative to the CERES estimate, as seen in the overall period means, is likely due to the undersampling of upper tropospheric clouds by the instrumentation at Gan and its impact on the CombRet radiative calculations. For example, on days with high cloud fraction less than the

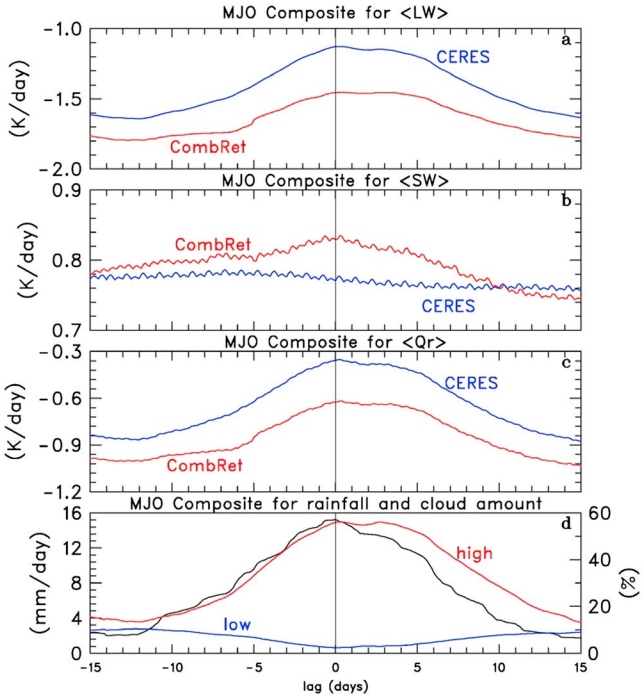

Figure 4. MJO composite lifecycle of various LP-filtered all-sky fields: (a) <SW>, (b) <LW>, (c) $<Q_r>$ from CombRet (red) and CERES (blue), and (d) TRMM rainfall (in black with scale to left), and high (red) and low (blue) cloud amount with scale to right. Fields were composited around peak LP-filtered rainfall times shown in Figure 2 for the period of 1 October to 31 December 2011.

period mean of 32%, the $<Q_r>$ offset is 0.14 K/d, whereas on days with high cloud fraction greater than the mean, the CERES $<Q_r>$ is 0.28 K/d greater than the CombRet value.

While the deficiencies in the CombRet estimates produce a cooling bias during periods with abundant high cirrus, one must also consider the sensitivity of the CERES radiative transfer computations to biases in the MERRA analysis fields. For example, as noted earlier, upper level humidity has been shown to be excessively high in model analyses compared to sounding observations over the IO (indicative of excessive cirrus coverage in the reanalyses [*Ciesielski et al.*, 2014]). This may result in a small positive heating bias in the CERES estimates over this region and partially compensate for the effects of missing thin cirrus in the CERES retrievals noted earlier (DC15). In short, the true column-net radiative heating/cooling rates are likely bracketed by the CombRet and CERES radiative estimates.

A composite analysis based on LP rainfall for the convectively active period covering the three MJO events from 10 October to 31 December is shown in Figure 4 for the column-averaged all-sky CombRet and CERES LP-filtered fields. Here day 0 represents the peak in LP rainfall with negative (positive) lag days being prior to (after) this rainfall peak. The <SW> fields (Figure 4b) exhibit a slight variation (amplitude < 0.1 K/d) over the MJO lifecycle with the CombRet having a weak heating peak near day 0. This heating peak is likely an artifact due to the lack of high clouds in the CombRet retrieval since LM04 found a weak <SW> minimum near the time of peak rainfall, which they attribute to high clouds reducing shortwave absorption. The CERES <SW> behavior shows a slight minimum following the rainfall peak and appears more in line with LM04. The <LW> (Figure 4a) and $<Q_r>$ (Figure 4c) fields display a broad cooling minimum at and following the rainfall peak consistent with the variations in high cloud amount. This corroborates the findings of LM04 based on different data sets over the west Pacific warm pool region, which found that $<Q_r>$ lagged convective heating by less than 5 days. The amplitude of the all-sky $<Q_r>$ variation over the MJO lifecycle is 0.52 (0.42) K/d in the CERES (CombRet) data.

To further explore the relationship between radiation and convection, Figure 5 presents the time series of the LP-filtered radiative fields as function of height for all-sky, clear-sky, and CRF conditions. Focusing first on the all-sky results (Figure 5, left column), the LW cooling field (Figure 5, top row) shows a tilted structure, associated with the prevalence of shallow cumulus during the dry suppressed MJO phase, followed by increasing deep convection leading into the active phase. LW cooling maximizes at low levels during the dry periods and at upper levels following periods of heavy rainfall with peak rates approaching −3 K/d. The enhanced cooling peaks aloft, related to increased LW cooling atop upper level clouds, should likely be shifted to higher altitudes due the underestimation of high-level cloudiness in the CombRet product [*Feng et al.*, 2014]. Using comparisons between the various radars on Gan, their study indicated that the average cloud top underestimation due to KAZR attenuation by rainfall during the DYNAMO/AMIE field campaign was 1.15 km.

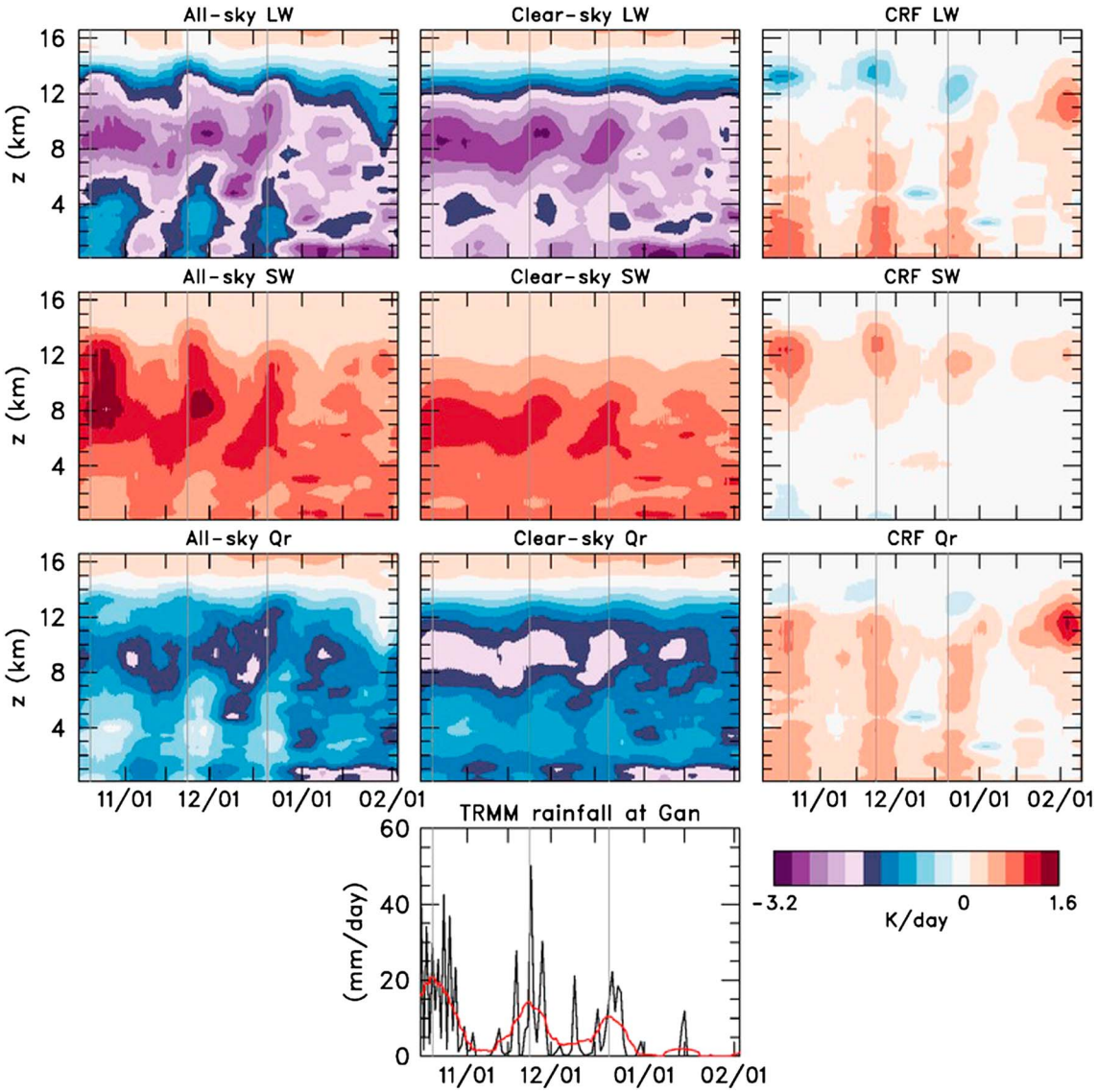

Figure 5. (top to bottom) Height-time series of LP-filtered CombRet LW, SW, and Q_r, respectively; (left to right) for all-sky, clear-sky, and CRF conditions, respectively, and (bottom-middle) Gan rainfall (black curves and red lines as in Figure 2). Thin vertical lines denote LP-filtered rainfall peaks for each MJO.

Tilted structures are also seen in the all-sky SW heating field associated with changes in the convective population through the course of the MJO as described above. Peak SW heating rates, on the order of 1.5 K/d, occur near 8 km (~400 hPa) during periods of deep convection. The combination of these LW and SW effects results in reduced all-sky Q_r cooling, even reverting to small net-heating at times in the midtroposphere (3–5 km) during the convectively active phases of the MJO.

The corresponding clear-sky and CRF height-time analyses are shown in Figure 5 (middle and right columns). Despite the minimal temporal variations in the column-averaged clear-sky radiative fields (Figure 2), the clear-sky vertical profiles exhibit considerable variation and vertical tilting in time. In contrast, the CRF fields show little vertical tilt and smaller magnitudes. In addition, the LW cooling and SW heating peaks in the CRF fields are shifted upward several kilometers relative to their clear-sky counterparts with the CRF fields being more sensitive to changes in high cloudiness and the clear-sky fields being more sensitive to variations in the midlevel moisture gradient. Focusing on the CRF fields, periods of heavy rainfall are associated with LW cloud top cooling between 12 and 14 km and SW heating immediately below this level with strong LW heating at low levels. In contrast to rainy periods, upper level LW heating was prominent during the late January to early February period, which was characterized by abundant high cloudiness (Figure 3a) but little to no

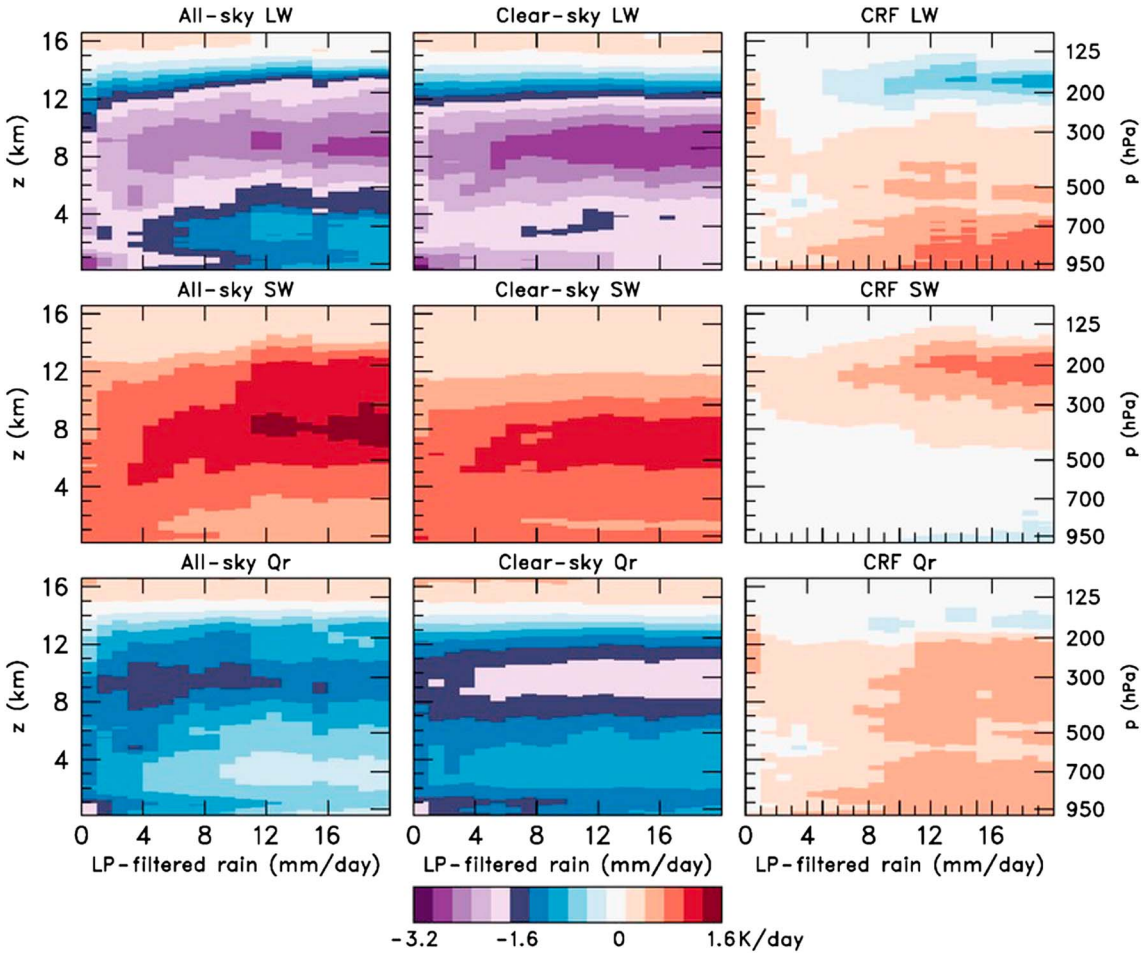

Figure 6. Low pass-filtered radiative fields (top to bottom) LW, SW, and Q_r, respectively, composited by LP-filtered rain rate based on period 10 October 2011 to 08 February 2012 for (left to right) all-sky, clear-sky, and CRF conditions, respectively.

precipitation near Gan. This period was presumably dominated by thin cirrus, hence radiative heating of the cloud layer itself [e.g., *Webster and Stephens*, 1980; *Ackerman et al.*, 1988].

To better quantify how these radiative fields vary with rain rate, Figure 6 shows them composited by LP-filtered Gan rain rate. First, we consider the clear-sky results (Figure 6, middle column). At low levels, strong LW cooling at low rain rates transitions to weak cooling at higher rain rates. At upper levels, cooling centered in 8–10 km layer (~300 hPa) gradually increases as rain rates increase. In the SW, heating rates gradually increase in magnitude and elevation with increasing rain rate with peak rates in the 6–8 km layer. In terms of Q_r, the overall pattern is similar to that of the LW. Interestingly, the upper level cooling peak in all-sky Q_r (−1.5 K/d) occurs at modest rain rates of 3–6 mm/d due to the greater cancellation of SW heating and LW cooling at higher rain rates.

The composite analyses of the CRF effects (Figure 6, right column) show a ramp-up in upper level cloud top SW positive CRF near 200 hPa, LW negative CRF slightly above this level, and low-level LW positive CRF as rain rates increase. Although there is prominent upper level SW positive CRF, it is accompanied by weak SW negative CRF below 6 km resulting in the small column-net SW CRF effects seen in Figure 2b. Weak cloud top LW negative CRF is also noted around 4.5 km at lighter rain rates, presumably due to trade-cumulus and congestus cloud populations.

Due to differences in the evolution of convection during the various stages of the MJO [e.g., *Mapes et al.*, 2006; DC15], we have separated the composite analyses into periods of developing or decaying MJO convection (i.e., times with increasing and decreasing MJO rainfall). Overall, the period differences are small (not shown) with the main distinction being a gradual rise in the elevation of the peak LW cooling and SW

At upper levels (12–14 km), the downward tilted positive LW anomaly signature seen between days −15 to −5 may be a consequence of thin cirrus during that period [*Del Genio et al*., 2012; DC15] and/or downward propagating Kelvin waves [*Virts and Wallace*, 2014], or in part may simply be a reflection of the strong negative anomalies associated with abundant cirrus in the MJO active phase. This warming transitions to a strong cooling signature (~0.6 K d^{-1}) due primarily to CRF effects associated with abundant high clouds which maximize in 5 days following peak rainfall. The upper level SW fields show an opposite trend to the LW with deeper but weaker anomalies. While the upper level CRF anomalies are primarily confined to above 12 km, the contribution of the clear-sky fields result in upper level all-sky LW and SW anomalies which extend downward to 8 km, suggesting the important role of water vapor in producing these deeper radiative signatures.

In general, the all-sky Q_r signature of the MJO (Figure 7, bottom left) is dominated by LW effects with some modification from the SW with anomalies that are smaller and generally of opposite sign to the LW. Q_r positive anomalies range from 0.3 to 0.5 K/d, peaking at low levels near lag 0 then gradually become top-heavy in the days following the rainfall peak. These anomalies, based on a 3-MJO composite, are only slightly larger that those found in the 10-MJO composite of DC15 (0.2–0.4 K/d). Considering all the sampling difference in space and time between these studies, the overall radiative anomaly patterns in terms of vertical tilt and magnitude are remarkably similar.

3.2. Convective Context for Radiative Fields

To better understand the nature of convection and its relationship to radiative fields in the vicinity of Gan during this period, we now examine the AMIE-GAN large-scale atmospheric budget analyses, which represent an average in a circular area with a 150 km radius centered on Gan Island (see Figure 1). The time series of relative humidity RH, apparent heat source Q_1, and apparent moisture sink Q_2 from these analyses are shown in Figure 8 for the period of 2 October to 31 December 2011. These fields have been temporally smoothed by application of a 5 day running-mean filter to daily-averaged values. Also shown in Figure 8 (bottom two plots) are time series of daily-averaged stratiform rain fraction and the adjusted-SMART-R rainfall. The MJO heavy-rain periods are accompanied by pronounced increases in RH, in the amplitudes of Q_1 and Q_2 and in the stratiform rain fraction. The evolution of these fields through all three MJOs exhibits a similar progression to that documented by *Lin and Johnson* [1996] in TOGA COARE. In each case, shallow nonprecipitating cumulus indicated by low-tropospheric moistening (negative Q_2) during the convectively suppressed phase is followed by cumulus congestus (with low-level to midlevel peaks in Q_1 and Q_2), then deep convection with higher and stronger peaks in Q_1 and Q_2, and finally stratiform-like profiles with positive peaks aloft and negative peaks at low levels.

While this progression of convection is similar for all three MJO events, the intensity and duration of the different convective stages vary among the events. For example, the low-level moistening is strongest prior to the October MJO active period which has the longest duration of heating and drying signatures, the stratiform signal is most prominent following the November MJO, and the heating and drying signatures are weakest in the December MJO. These differences likely contribute to the radiative differences among the MJOs as seen in Figures 2 and 5. As noted in *Xu and Rutledge* [2016], the shallow-to-deep convective transition (SDT) times during DYNAMO (<7 days) were on the shorter end of the SDT spectrum with nearly 50% of 74 MJOs they examined having SDT time scales of 10–20 days.

Vertical profiles of Q_1 and Q_2 for these different convective stages are presented in Figure 9 (top row) where the averaging periods for the various stages are defined as in *Ruppert and Johnson* [2015, Figure 2] and are shown between the second and third panels of Figure 8. These profiles are based on the 10 October to 31 December period to overlap the CombRet data period such that the early-October suppressed period was not included in these analyses. In Figures 8 and 9 SP refers to suppressed periods, BH to bottom-heavy convection with heating/drying peaks below the 0°C level (~550 hPa), DC to deep convection, and SF to periods with predominately stratiform-type convection. While all types of convection may occur within a given period, these classifications identify the dominant mode of convection within that period. The SP profiles resemble those found in trade cumulus environments [*Nitta and Esbensen*, 1974; *Johnson and Lin*, 1997] with negative values of apparent drying Q_2 at lower levels (900–500 hPa) reflecting the important moistening effects of shallow, nonprecipitating clouds. Due to the sensitivity of deep convection to midlevel moisture [*Wang and Sobel*, 2012; *Powell*, 2016], the midlevel moistening observed during the BH period

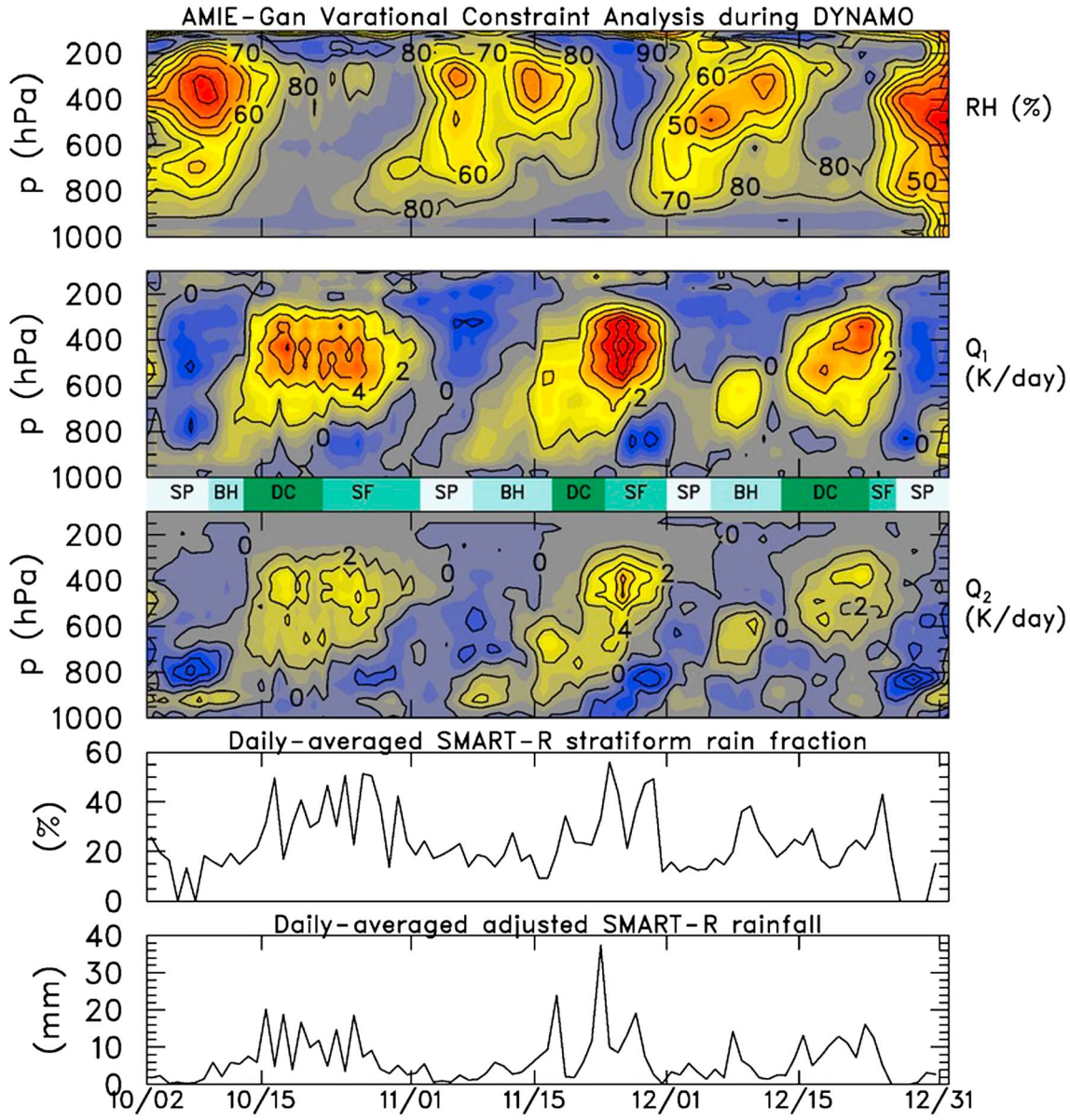

Figure 8. (top to bottom) Height-time plots of AMIE-Gan 5 day running mean of daily fields: RH, Q_1, Q_2, and daily-averaged time series of stratiform rain fraction, and adjusted-SMART-R rainfall. Contour increment is 10% for RH and 2 K/d for Q_1 and Q_2. The green shading between second and third panels denotes various convective periods: SP = suppressed, BH = bottom heavy, DC = deep convective, SF = stratiform.

(i.e., negative values of Q_2 between 550 and 300 hPa) results in a more favorable environment essential for the development of deep convection going into the active phase of the MJO [*Powell and Houze*, 2015]. The profiles going from left to right in Figure 9 indicate an increasing stratiform rain fraction (SRF with period-mean values listed in bottom right corner of panels) with little stratiform convection in SP to it being largest during the SF period when both stratiform and convective modes contribute to profiles characterized by top-heavy heating and drying, strong vertical heating gradients at midlevel with cooling and moistening below 800 hPa [*Schumacher et al.*, 2004]. These higher SRFs during the active phase of the MJO are consistent with the findings of *Lin et al.* [2004] and *Jiang et al.* [2011]. We also note that limitations in the *Steiner et al.* [1995] convective-stratiform classification algorithm, especially during periods of shallow convection, result in SRFs too high during the SP and BH periods [*Powell et al.*, 2016]. Their analysis suggests that SRFs should be near 0% during the SP periods. Finally, as one might expect, rainfall (with period-mean values in bottom right corner of panels) is a minimum during SP and increases nearly fivefold maximizing in the DC and SF periods.

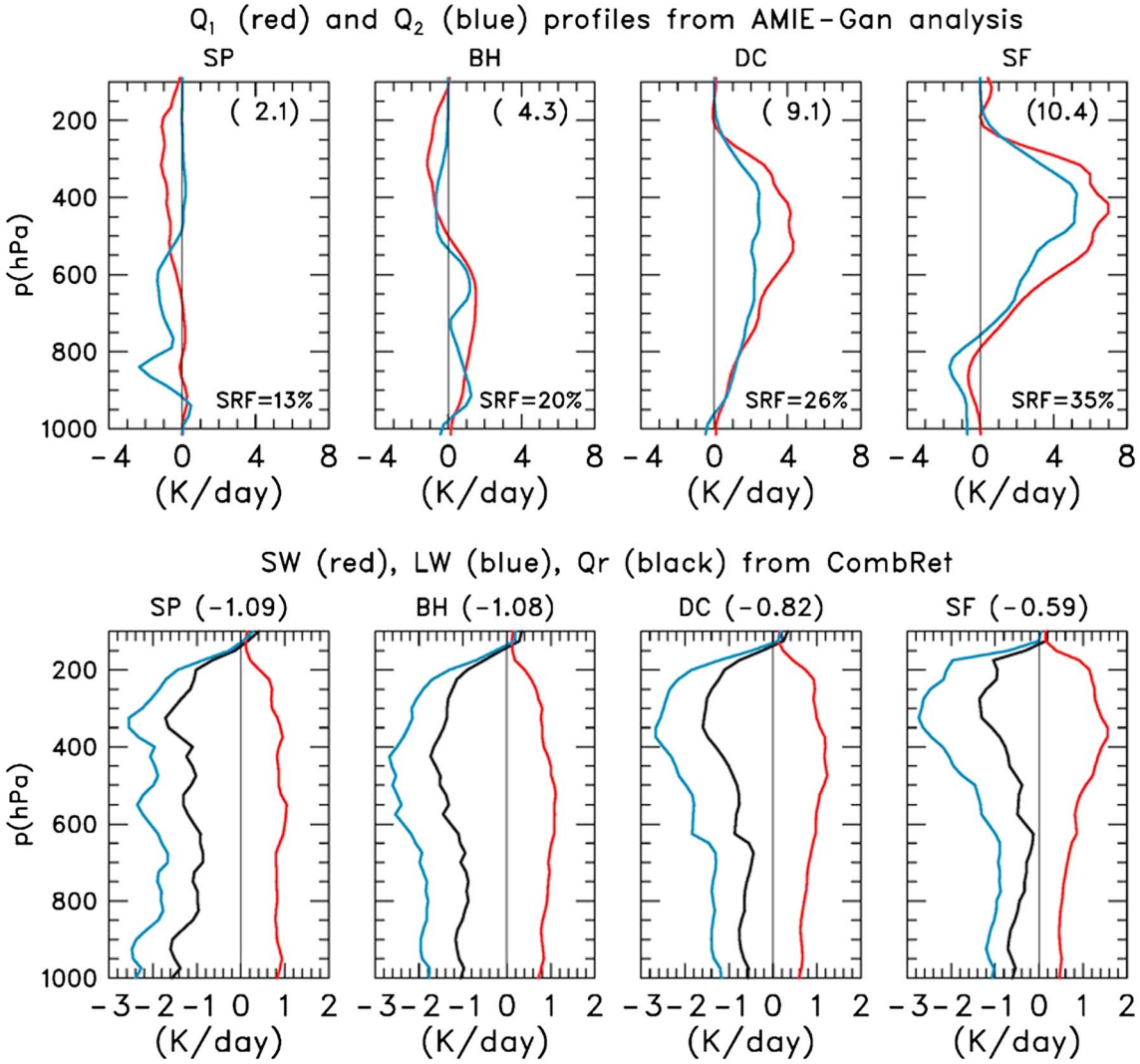

Figure 9. (top row) Mean vertical profiles for Q_1 (red) and Q_2 (blue) for four convective periods: (from left to right) SP, suppressed; BH, bottom heavy; DC (deep-convective) and SF (stratiform). See text for additional details concerning periods. Numbers in parentheses in bottom right corner show mean SMART-R TRMM-adjusted rain rate (mm/d) for each period. The mean stratiform rain fraction (SRF) for each period is listed in the bottom right corner. (bottom row) As in the top row except vertical profiles for CombRet radiative fields SW (red), LW (blue), and Q_r (black). Mean $<Q_r>$ in K/d for each period is given in parentheses at top of plots.

The radiative profiles associated with these convective periods are shown in Figure 9 (bottom row). The SP period is characterized with a vertically deep Q_r cooling profile, which peaks at low levels, a consequence of strong LW cooling under dry, suppressed conditions. As the convection builds going into the MJO active phase the radiative profiles become increasingly top-heavy (i.e., characterized by an upper level cooling maximum) with $<Q_r>$ progressively decreasing. The variation of $<Q_r>$ between these periods (0.5 K/d) is consistent with the intraseasonal variation in this field found in Figures 2c and 4c. Peaking between 400 and 200 hPa, the strongest SW heating (with rates approaching 1.5 K/d) and LW cooling (~3 K/d) occurred during the SF period. Also during this period, Q_r has a distinct cooling peak near 325 hPa with a midlevel minimum. Cumulus ensemble simulations of tropical cloud clusters have shown that this type of Q_r profile is conducive to destabilization of upper level stratiform anvils, which contributes to their greater extent and longevity [*Fu et al.*, 1995].

To complement the radiative MJO composites in Figure 7, a similar composite for the AMIE-Gan fields is shown in Figure 10. The convective regimes discussed above occur roughly from days −15 to −10 for SP, days −10 to −5 for BH, days −5 to +1 for DC, and days +1 to +9 for SF. Below 13 km, the peak temperature anomaly occurs at the time of peak rainfall, presumably related to latent heating effects of deep convection

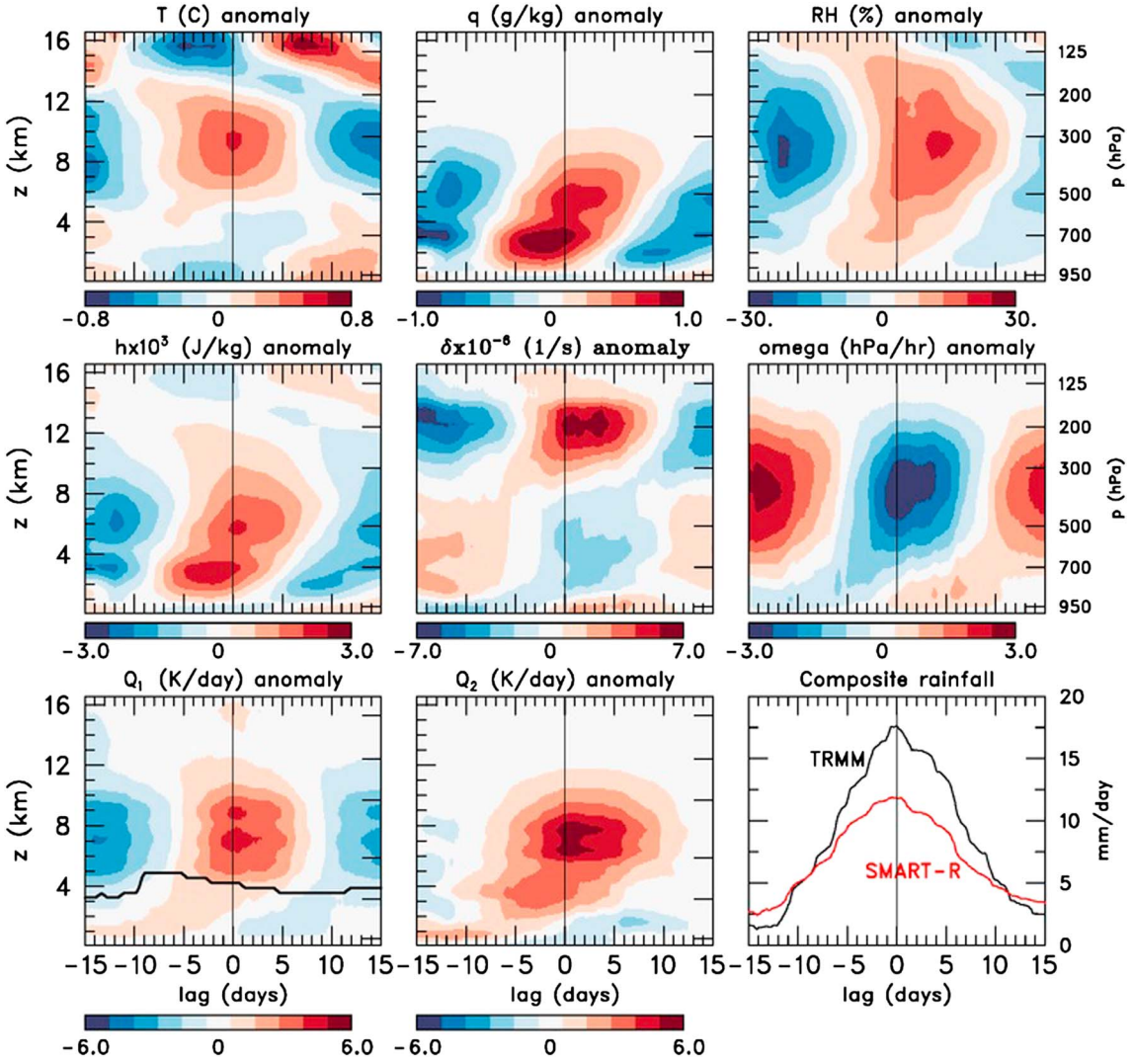

Figure 10. Composite anomalous atmospheric fields as a function of lag relative to the MJO peak rainfall based on LP-filtered AMIE-Gan analyses: (top row) temperature, specific humidity, and relative humidity; (middle row) moist static energy, divergence, and omega; (bottom row) apparent heating, apparent drying, and LP-filtered rainfall. The thin vertical lines denote lag 0 when MJO rainfall was a maximum. The heavy solid line in bottom left plot represents the level of *h* minimum.

consistent with the peak in the Q_1 composite. The coincidence between the upper level tropospheric warm anomaly and rising motion seen throughout much of the MJO lifecycle is indicative of a disturbance converting available potential energy to kinetic energy [*Yanai et al*., 2000; *Kiladis et al*., 2005]. At low levels, weak warm anomalies and convergence associated with shallow convection during the SP transition to cool anomalies and deep-layer convergence as convection strengthens and rain rates increase. The deep cool anomaly extending from the surface to ~5 km after day 0 is associated with evaporative cooling from stratiform convection which increasingly predominates during this period. This is consistent with the heating (drying) anomalies atop cooling (moistening) anomalies seen during the SF period in the Q_1 and Q_2 fields, respectively. The vertically tilted specific humidity field reflects the changes in cloud populations and strongly impacts the structure of the moist static energy ($h = c_pT + g_z + Lq$) anomalies below 10 km. Above 13 km, tilted temperature and RH anomalies are consistent with signatures of downward propagating Kelvin waves [*Virts and Wallace*, 2014; *Kiladis et al*., 2005].

To better quantify the evolution of the large-scale fields as a function of rainfall intensity, Figure 11 shows a composite of these fields by LP-filtered rain rate for all periods (Figure 11, left column) as well as for periods with increasing MJO rainfall (Figure 11, middle column) and decreasing MJO rainfall (Figure 11, right column). For the latter two composites, the convectively suppressed periods have not been included. Focusing first on

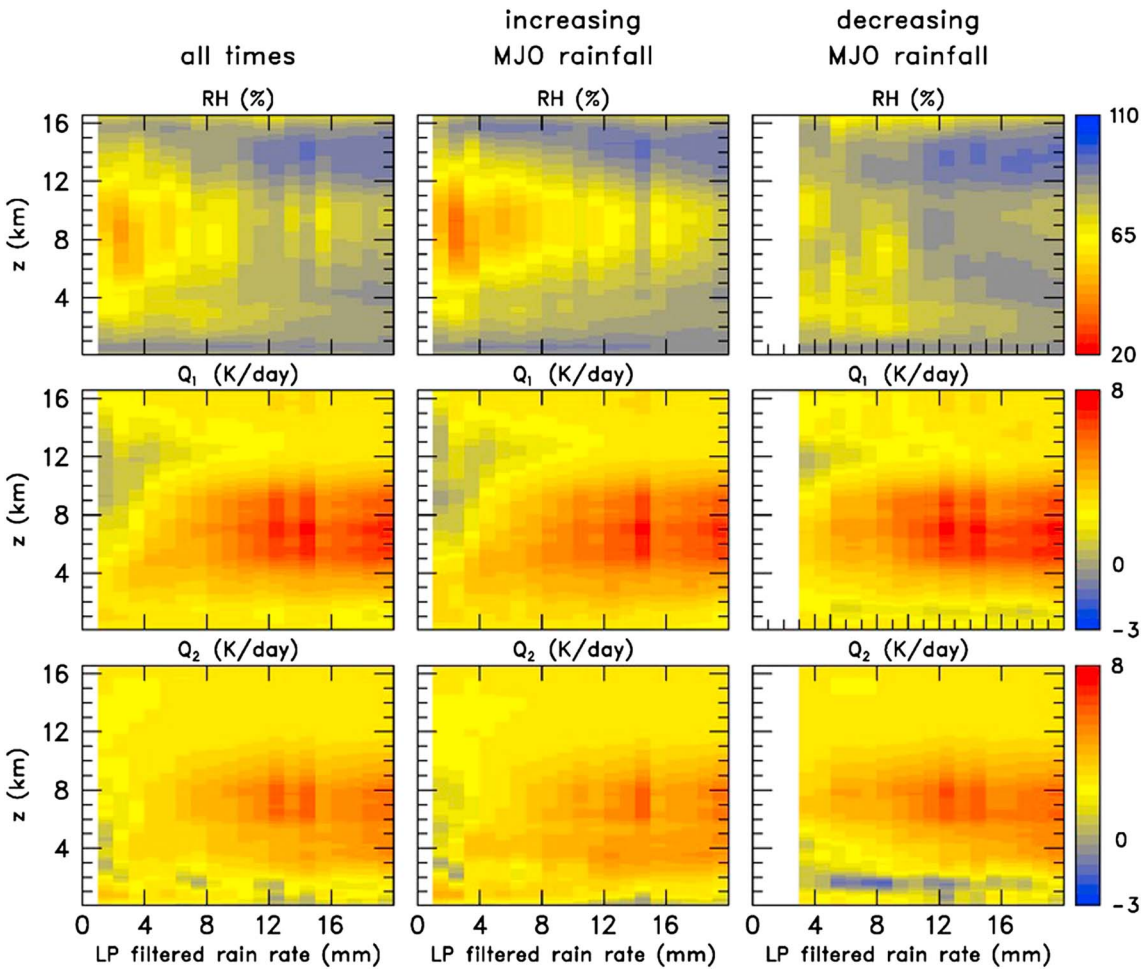

Figure 11. Low pass-filtered AMIE-Gan analyses composited by LP-filtered rain rate based on the period of 2 October 2011 to 31 December 2011. (top row) RH, (middle row) Q_1, and (bottom row) Q_2 (left column) for all times, (middle column) for times with increasing MJO rainfall, and (right column) for times with deceasing MJO rainfall. Suppressed periods as defined in Figure 8 are not included in the middle and right column composites.

Figure 11 (left column) (i.e., all-period composite), at low rain rates, profiles are characterized by dry midlevels, weak and shallow convective heating and moistening, and enhanced low-level LW cooling (Figure 6). As rain rates increase, the midlevels moisten and the heating/drying rates ramp up with peak values between 5 and 9 km. Contributing to the structure, the Q_1 field, SW heating due to absorption within the clouds peaks around 8 km while strong LW cooling is observed near 10 km (Figure 6). At the higher rain rates, a secondary maximum in Q_2 forms near 4 km. This vertical separation of peaks in Q_1 and Q_2 is consistent with the idea of increasing convective eddy fluxes associated with heavy rainfall [*Yanai et al.*, 1973]. This vertical separation is most evident at higher rain rates for increasing MJO rainfall (Figure 11, bottom middle) when deep convection would be present. Comparing the increasing versus decreasing rainfall composites, the following differences are noted. The increasing rainfall period shows a gradual deepening of convection with rain rate indicative of a transition from shallow to deep convection with drier conditions at midlevels for light rainfall. Also, the greater low-level cooling (negative Q_1) and moistening (negative Q_2) for decreasing MJO rainfall suggests the predominance of stratiform rainfall during this period.

3.3. Assessment of Radiative-Convective Instability

Previous studies [*Raymond*, 2001; *Lee et al.*, 2001] have found that if the ratio of the anomalous column-integrated net-radiative heating $<Q_r>$ to anomalous column-integrated convective heating $<Q_{conv}>$, also referred to as the radiative heating enhancement factor (EF) in LM04, is greater than 20%, gross moist stability goes to zero such that a radiative-convective instability could result in MJO-like modes [*Yu et al.*, 1998]. On the other hand, *Sobel and Maloney* [2012, 2013] hypothesize that the existence of radiative-convective instability

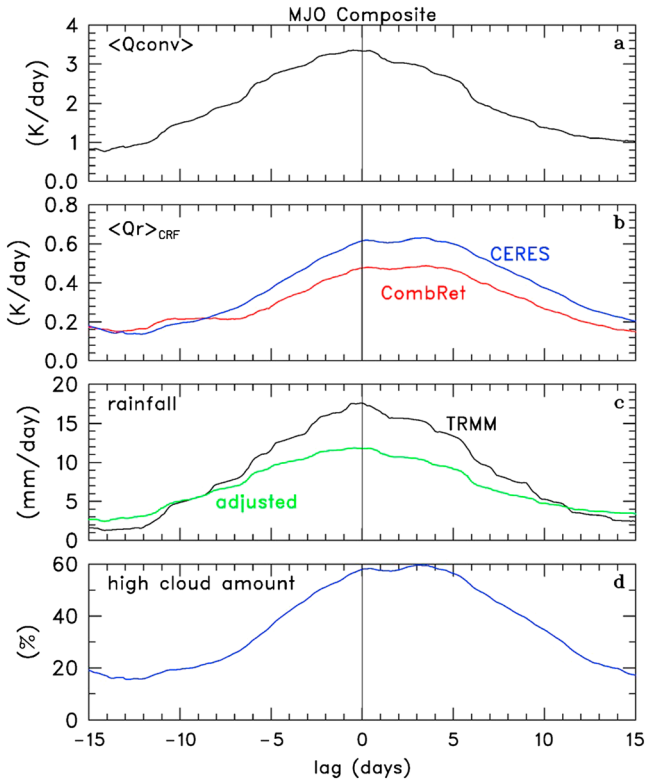

Figure 12. MJO composite lifecycle as function of lag relative to MJO rainfall peak for (a) $<Q_{conv}>$ from AMIE-Gan analyses, (b) $<Q_r>_{CRF}$ from CombRet (red) and CERES (blue), (c) TRMM rainfall (black) and adjusted-SMART-R rainfall (green), and (d) high cloud amount (blue) cloud amount. Fields were composited around peak LP-filtered rainfall times shown in Figure 2 for the October and November MJOs.

is dependent not just on the EF but also its size in relation to normalized gross moist stability (NGMS). Specifically, they posit that if EF is greater than NGMS, then such an instability can exist. Physically, exceeding this critical ratio means that radiative heating increases the moist static energy in the column faster than the vertical motion and associated circulation can export it. Using data averaged over the northern sounding array of DYNAMO, *Johnson et al.* [2015] found EFs occasionally exceeding 20% and comparable to the NGMS values reported by *Sobel et al.* [2014] leaving open the possibility of radiative-convective instablity for the MJOs in DYNAMO. We now revisit this EF computation by using the high-quality DYNAMO data sets over the Gan region.

Figure 12 shows an MJO composite of the following LP-filtered fields: $<Q_{conv}>$, estimates of $<Q_r>_{CRF}$ from CERES and CombRet, rain rates from TRMM and adjusted-SMART-R, and high cloud amount. Here and in subsequent analyses, $<Q_{conv}>$ as defined in equation (2) was computed as $LP_o + S$, where P_o came from the adjusted SMART-R rainfall and S from ECMWF analyses. The compositing for this plot was restricted to the October and November MJOs because the length of the AMIE-Gan LP analyses, which were available only through 25 December, was unable to fully sample the December MJO. Several noteworthy features are present in this figure. First, a broad peak in the $<Q_r>_{CRF}$ signal lags the $<Q_{conv}>$ peak by a few days (also seen in Figure 4) and the ratio of the range (i.e., maximum minus minimum difference) of $<Q_r>_{CRF}$ to the range of $<Q_{conv}>$ is 16% (21%) for the CombRet (CERES) estimates. Here the $<Q_{conv}>$ range is 2.6 K/d. While this lag compares reasonably well to that shown in LM04, these ratios are slightly larger than the 10–15% which they found. Next, we note that the CombRet and CERES $<Q_r>_{CRF}$ estimates are closer in magnitude for negative lag days when the high cloud amount was <20%. However, for large values of high cloud fraction, CERES estimates exhibited ~0.15 K/d more heating than CombRet. As noted earlier, the true radiative heating/cooling rates are likely bracketed by these two radiative estimates. Finally, we note in Figure 12c that the rain rates for adjusted SMART-R are greater than TRMM by nearly a factor of 2 at rain rates <4 mm/d and up to 40% less than TRMM at the highest rates. This

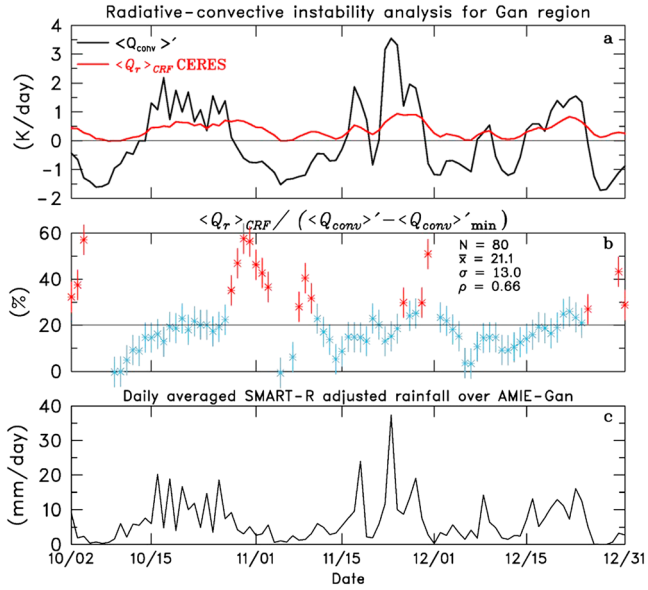

Figure 13. Time series of 3 day running-mean daily values of (a) $<Q_{conv}>'$ (black), CERES $<Q_r>_{CFR}$ (red); (b) enhancement factor (EF) using CERES data with 95% confidence interval (short vertical lines where red symbols and vertical lines indicate EF values that are above the 20% threshold at a 95% significance level; blue symbols are not significant at this level); and (c) daily-averaged adjusted-SMART-R rainfall. The 20% ratio line is shown in Figure 13b; ratios greater than this value signify that the condition for radiative-convective instability is satisfied. See text for additional details concerning these analyses.

corroborates the finding of *Xu and Rutledge* [2014], based on radar data from R/V *Revelle*, where they found that TRMM 3B42 rainfall product *underestimates* rainfall during suppressed periods (presumably due to insufficient sampling of shallow, warm-rain clouds) and *overestimates* rainfall during convectively active periods (likely due to abundance of high-level cloudiness). Similar biases in the TRMM rainfall estimates were noted between the time series of TRMM 3B42 and budget-derived rainfall estimates over the larger DYNAMO sounding arrays [*Johnson et al*., 2015, hereafter J15].

To examine the temporal behavior of the radiative heating EF as in J15, we show in Figure 13a the time series of anomalous $<Q_{conv}>$ and $<Q_r>_{CRF}$ and their ratio (Figure 13b), along with the SMART-R-adjusted TRMM rainfall (Figure 13c). Following J15, convective anomalies (denoted with a prime in formula below) were computed by subtracting their temporal mean and the EF ratio was computed as follows:

$$EF = < Q_r >_{CRF} / (< Qconv > ' - < Qconv > '_{min}) \quad (3)$$

where $< >_{min}$, representing the minimum value in the time series, was used to ensure nonnegative values in the denominator of equation (3). To avoid times where the denominator in equation (3) approaches zero, ratios are only plotted for daily rain rates >1 mm/d. For this analysis the CERES $<Q_r>_{CFR}$ data are preferred over the CombRet product since the former is an area average (as opposed to the point CombRet measurements) and shows less adverse effects related to issues with missing high cloudiness. As one would expect, $<Q_{conv}>'$ closely resembles the rainfall behavior with radiative peaks generally occurring a few days after convective heating peaks. For days with rain rates >1 mm/d, the mean EF is 21% which is consistent with the LM2004 speculation that ratios over IO could be higher than the 10–15% they found over the West Pacific. Error bars in Figure 13b indicate the 95% confidence interval based on two-sided Student's *t* test [*Wilks*, 1995]. The red error bars indicate EF values that exceed the 20% threshold at a 95% confidence level. Of special note is the extended period with large EF (>30%) during the late-October to early-November period, which suggest that conditions for radiative-convective instability were present helping to maintain the MJO as it moved eastward.

In J15 $<Q_{conv}>$ was computed as $<Q_1> - <Q_r>$, where $<Q_1>$ was computed from the large-scale budget analyses over the NSA and $<Q_r>$ came from CERES data. Because the R/V *Revelle* (ship at southeast vertex of NSA) was in port during the late October/early November period (shaded region in Figure 13 of J15), the budget results used to compute $<Q_{conv}>$ were less reliable during this time. Thus, the radiative-

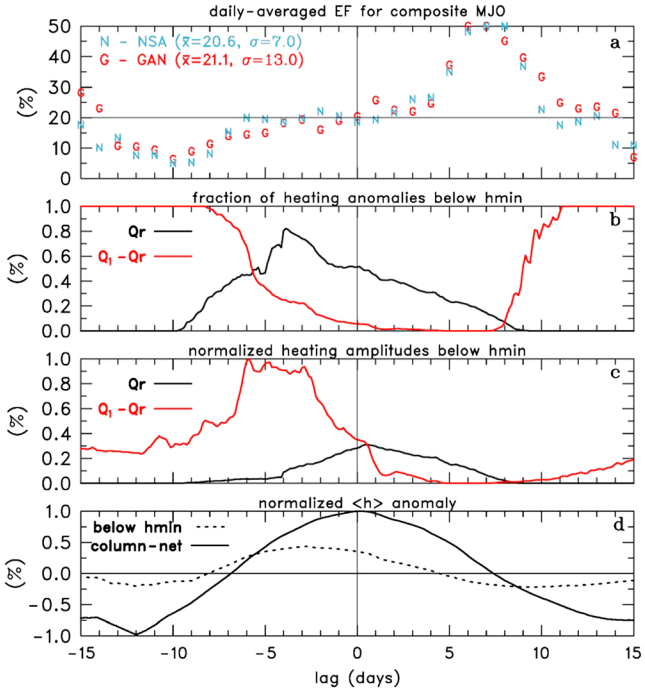

Figure 14. MJO composite lifecycle as a function of lag relative to MJO rainfall peak for (a) daily-averaged enhancement factor (EF) using AMIE-Gan (red G symbol) and NSA (blue N symbol) analyses, where numbers in parentheses indicate mean and standard deviation of EF time series and the 20% critical threshold line is also shown (to better capture the variability of EF over the MJO lifecycle, values of EF > 50% are capped at this level); (b) fraction of positive heating anomalies (radiative—black, convective—red) below h_{min}; (c) as in Figure 14b except magnitude of heating anomalies normalized by largest value; (d) column-integrated h anomaly normalized by largest value for column-net (solid) and contribution to $<h>$ from below h_{min} (dotted).

convective instability analysis for the NSA is recomputed here in a similar fashion as to what was done for the Gan region. The SMART-R versus TRMM rainfall relationship from the Gan region (not shown) was applied to scale the NSA-averaged TRMM rainfall to obtain an adjusted rainfall P_{adj} used to compute $<Q_{conv}> = LP_{adj} + S$, where S is from ECMWF analysis. The revised NSA EF time series (not shown) has statistically significant ratios greater than 20% after each MJO event similar to those for the Gan region.

Compositing the daily-averaged EF values for the Gan and NSA regions based on MJO rainfall (Figure 14a), a similar pattern emerges for both areas with a minimum in EF around day −10, a gradual increase from day −10 to day +4, then a rapid increase to maximum centered around day +7. This suggests that as MJO convective envelope weakens over the central IO, cloud-radiative feedbacks help maintain the mature MJO as it moves eastward [*Adames and Kim*, 2016]. The smaller standard deviation of EF values for the NSA (listed in Figure 14a) is expected from sampling theory, as the area of the NSA over which the fields are being averaged is about 5 times the area of the AMIE-Gan domain. While assigning statistical significance to the EF values in Figure 14a is difficult due to the small composite sample size of three MJOs, we note that for both regions the EF minima around day −10 are more than 1σ below the critical threshold while the maxima around day +7 are greater than 2σ above this threshold. Furthermore, a similar EF variation over the MJO lifecycle can be surmised from satellite analyses in DC15, as well as in the *Kim et al*. [2015] study, which found peak EF values in weak precipitation regimes.

Recent studies such as *Ma and Kuang* [2011] and DC15 have noted that in addition to the column integral of Q_r, the vertical distribution has important implications on the h-budget. As discussed in these studies, the divergent circulation's response to positive Q_r anomalies concentrated in the lower troposphere (specifically below h_{min}, i.e., the vertical level of moist static energy miminum) will result in an import of h into the column and further enhancement of convection. The opposite is true for positive Q_r anomalies above h_{min}. During the time period of maximum EF in Figure 14a, the peak radiative anomalies have risen to midlevels (as seen lower left panel of Figure 7), which is clearly above h_{min} also shown in Figure 7.

To explore this point further, the remaining panels in Figure 14 consider additional details on how low-level radiative and convective heating ($Q_1 - Q_r$) anomalies vary over the course of a composite MJO. Figures 14b and 14c show the fraction and normalized magnitude of these heating anomalies which lie below h_{min}, respectively. During the suppressed phase, shallow convection results in small convective heating anomalies which lie entirely below h_{min}. As convection builds vertically going into the MJO active phase, the convective anomalies increase in magnitude between days −7 and −3, while their fraction below h_{min} diminishes. During these developing stages of the MJO, shallow and bottom heavy convection dominates the import of h at low levels . After day −5 radiative heating anomalies quickly ramp up and contribute to the import

h at low levels. Following the rainfall peak at lag 0, radiative anomalies dominate the enhancement of low level h. Column integrated h $<h>$ peaks near lag 0 (Figure 14d, solid curve) with a significant contribution to its increase during the MJO developing stages coming from the circulation's response to low-level heating anomalies (dashed curve). After day 0, the radiative anomalies become increasingly top heavy, which act in the direction of exporting h at upper levels.

4. Summary and Conclusions

Radiative heating rates computed over Gan Island region in the central Indian Ocean are used along with a variational constraint analyses of large-scale fields centered on this location to examine the relationship between radiation, clouds, and convection on an intraseasonal time scale using data taken during the DYNAMO field campaign. During the 3 month period (October to December 2011) three MJO events occurred over this region.

The principal findings of this study are as follows:

1. Time-height plots of longwave and shortwave radiation exhibit tilted structures, reflecting radiative effects associated with the prevalence of shallow cumulus during the dry, suppressed MJO phase followed by increasing deep convection leading into the active phase.
2. While both the water vapor and cloud fields are inextricably linked, it appears that the tilted radiative structures are more related to water vapor effects.
3. As the convection builds going into the MJO active phase, the radiative profiles are characterized with increasingly top-heavy anomalous radiative heating rates, while tropospheric-net radiative cooling rates $<Q_r>$ progressively decrease even reducing to near zero during periods with high-cloud coverage.
4. Temporal variations in the cloud radiative forcing (CRF) component of $<Q_r>$ are dominated by LW effects with an intraseasonal amplitude 0.42 K/d in CombRet and 0.54 K/d in CERES data. Due to measurement issues with both of these of products, these estimates likely bracket the true $<Q_r>$ modulation.
5. Intraseasonal variation of column-net radiative heating $<Q_r>$ lags column-net convective heating $<Q_{conv}>$ on the order of a few days and enhances the convective signal in the mean by 15–20%. This is generally consistent with the results of *Lin and Mapes* [2004], which were representative of the tropical west Pacific.
6. Radiative enhancement to convection is a minimum ~10 days prior to peak rainfall and maximizes around 1 week after the MJO rainfall peak. This suggests that as MJO convective envelope weakens over the central IO, cloud-radiative feedbacks help maintain the mature MJO as it moves eastward.

The veracity of the conclusions summarized above is subject to uncertainties, which are difficult to characterize, in both radiative and convective heating observations. While this study has used the most updated data sets available at the time of publication, the DYNAMO community is in the process of developing legacy data products. As part of this data legacy project, an improved radar rainfall data set with smaller uncertainties is being created by using a separate Z-R relationship for convective and stratiform rain (Brenda Dolan 2017, personal communication). Once this improved data set becomes available, the computations and conclusions herein should be revisited.

Results presented herein regarding radiative heating profiles as a function of rain rate may relate to processes regulating convection self-aggregation and its possible linkage to MJO physics, although details of the mechanisms are not obvious. Nevertheless, they will provide important validation for model representation of convective-radiative feedback under different convective regimes. For example, it will be interesting to explore how model fidelity in depicting the observed radiative heating versus rain rate relationship is related to the model fidelity in simulating the MJO based on multimodel simulations. In addition, composite radiative profiles during different MJO phases based on the Gan data during DYNAMO, including decomposition into moisture and clouds effects, will help identify model deficiencies in representing processes associated with radiation-convection feedbacks.

Acknowledgments

The authors thank three anonymous reviewers and Editor Chidong Zhang for their constructive comments that greatly improved this manuscript. We thank Zhe Feng of PNNL for generously providing the radiative heating profiles for Gan Island available at https://www.arm.gov/data/pi/71, the CERES radiation data were obtained from http://ceres.larc.nasa.gov/products.php?product=SYN1deg, the TRMM rainfall data were obtained from http://mirador.gsfc.nasa.gov/cgi-bin/mirador/presentNavigation.pl?tree = project&dataset = 3B42:%203-Hour%200.25%20x%200.25%20degree%20merged%20TRMM%20and%20other%20satellite%20estimates&project = TRMM&dataGroup = Gridded&version = 7&CGISESSID = 55fe8c1852563c116c65bac66a5fae85, and the AMIE-Gan variational analysis, which includes the adjusted-SMART-R rainfall data, can be found at http://www.arm.gov/news/data/post/28211. In addition, we thank Weixin Xu for making available the stratiform fraction data for the SMART-R radar (https://data.eol.ucar.edu/dataset/347.115), Chris Slocum for his assistant with the statistical testing, and Wayne Schubert, Weixin Xu, Brenda Dolan, and James Ruppert for many insightful discussions. This research was supported by the National Oceanic and Atmospheric Administration under grant NA15OAR4310177, by Department of Energy Grant DE-SC0008582, by the National Aeronautics and Space Administration under grant NNX13AF74G, and by the National Science Foundation (NSF) under grant AGS-1360237. Work at Lawrence Livermore National Laboratory (LLNL) was supported by the DOE Atmospheric Radiation Measurement Program (ARM) and performed under the auspices of the U.S. Department of Energy by LLNL under contract DE-AC52-07NA27344.

References

Ackerman, T. P., K. N. Liou, F. P. Valero, and L. Pfister (1988), Heating rates in tropical anvils, *J. Atmos. Sci.*, *45*(10), 1606–1623.

Adames, Á. F., and D. Kim (2016), The MJO as a dispersive, convectively coupled moisture wave: Theory and observations, *J. Atmos. Sci.*, *73*, 913–941.

Andersen, J. A., and Z. Kuang (2012), Moist static energy budget of MJO-like disturbances in the atmosphere of a zonally symmetric aqua-planet, *J. Clim.*, *25*, 2782–2804.
Arnold, N. P., and D. A. Randall (2015), Global-scale convective aggregation: Implications for the Madden-Julian Oscillation, *J. Adv. Model. Earth Syst.*, *7*, 1499–1518.
Arnold, N. P., Z. Kuang, and E. Tziperman (2013), Enhanced MJO-like variability at high SST, *J. Clim.*, *26*, 988–1001.
Bony, S., and K. A. Emanuel (2015), On the role of moist processes in tropical intraseasonal variability: Cloud–radiation and moisture–convection feedbacks, *J. Atmos. Sci.*, *72*, 2770–2789.
Ciesielski, P. E., et al. (2014), Quality controlled upper-air sounding dataset for DYNAMO/CINDY/AMIE: Development and corrections, *J. Atmos. Oceanic Technol.*, *31*, 741–764.
Coppin, D., and S. Bony (2015), Physical mechanisms controlling the initiation of convective self-aggregation in a general circulation model, *J. Adv. Model Earth Syst.*, *7*, 2060–2078.
Crueger, T., and B. Stevens (2015), The effect of atmospheric radiative heating by clouds on the Madden-Julian Oscillation, *J. Adv. Model Earth Syst.*, *7*, 854–864.
Del Genio, A. D., and Y. Chen (2015), Cloud-radiative driving of the Madden-Julian oscillation as seen by the A-Train, *J. Geophys. Res. Atmos.*, *120*, 5344–5356.
Del Genio, A. D., Y. Chen, D. Kim, and M.-S. Yao (2012), The MJO transition from shallow to deep convection in CloudSat/CALIPSO data and GISS GCM simulations, *J. Clim.*, *25*, 3755–3770.
DeMott, C. A., N. P. Klingaman, and S. J. Woolnough (2015), Atmosphere-ocean coupled processes in the Madden-Julian Oscillation, *Rev. Geophys.*, *53*, 1099–1154, doi:10.1002/2014RG000478.
DePasquale, A., C. Schumacher, and A. Rapp (2014), Radar observations of MJO and Kelvin wave interactions during DYNAMO/CINDY2011/AMIE, *J. Geophys. Res. Atmos.*, *119*, 6347–6367, doi:10.1002/2013JD021031.
Emanuel, K. A. (1987), An air-sea interaction model of intraseasonal oscillations in the tropics, *J. Atmos. Sci.*, *44*, 2324–2340.
Feng, Z., S. A. McFarlane, C. Schumacher, S. Ellis, J. M. Comstock, and N. Bharadwaj (2014), Constructing a merged cloud-precipitation radar dataset for tropical convective clouds during the DYNAMO/AMIE experiment at Addu Atoll, *J. Atmos. Oceanic Technol.*, *31*, 1021–1042.
Flatau, M., P. J. Flatau, P. Phoebus, and P. P. Niiler (1997), The feedback between equatorial convection and local radiative and evaporative processes: The implications for intraseasonal oscillations, *J. Atmos. Sci.*, *54*, 2373–2386.
Fu, Q., and K. N. Liou (1992), On the correlated k-distribution method for radiative transfer in nonhomogeneous atmospheres, *J. Atmos. Sci.*, *49*, 2139–2156.
Fu, Q., S. K. Krueger, and K. N. Liou (1995), Interactions of radiation and convection in simulated tropical cloud clusters, *J. Atmos. Sci.*, *52*, 1310–1328.
Gottschalck, J., P. E. Roundy, C. J. Schreck III, A. Vintzileos, and C. Zhang (2013), Large-scale atmospheric and oceanic conditions during the 2011–12 DYNAMO field campaign, *Mon. Weather Rev.*, *141*, 4173–4196.
Hamming, R. W. (1989), *Digital Filters*, 284 pp., Dover Publ., Mineola, New York.
Hartmann, D. L., M. E. Ockert-Bell, and M. L. Michelsen (1992), The effect of cloud type on the Earth's energy balance: Global analysis, *J. Clim.*, *5*, 1281–1304.
Holloway, C. E., and S. J. Woolnough (2016), The sensitivity of convective aggregation to diabatic processes in idealized radiative-convective equilibrium simulations, *J. Adv. Model Earth Syst.*, *8*, 166–195.
Hu, Q., and D. A. Randall (1994), Low-frequency oscillations in radiative-convective systems, *J. Atmos. Sci.*, *51*, 1089–1099.
Huffman, G. J., R. F. Adler, D. T. Bolvin, G. Gu, E. J. Nelkin, K. P. Bowman, E. F. Stocker, and D. B. Wolff (2007), The TRMM Multisatellite Precipitation Analysis: Quasi- global, multiyear, combined-sensor precipitation estimates at fine scale, *J. Hydrometeorol.*, *8*, 38–55.
Hung, M. P., J. L. Lin, W. Wang, D. Kim, T. Shinoda, and S. J. Weaver (2013), MJO and convectively coupled equatorial waves simulated by CMIP5 climate models, *J. Clim.*, *26*, 6185–6214.
Jiang, X., et al. (2011), Vertical diabatic heating structure of the MJO: Intercomparison between recent reanalyses and TRMM, *Mon. Weather Rev.*, *139*, 3208–3223.
Jiang, X., et al. (2015), Vertical structure and physical processes of the Madden-Julian Oscillation: Exploring key model physics in climate simulations, *J. Geophy. Res. Atmos.*, *120*, 4718–4748, doi:10.1002/2014JD022375.
Johnson, R. H., and P. E. Ciesielski (2000), Rainfall and radiative heating rates from TOGA COARE atmospheric budgets, *J. Atmos. Sci.*, *57*, 1497–1514.
Johnson, R. H., and P. E. Ciesielski (2013), Structure and properties of Madden–Julian Oscillations deduced from DYNAMO sounding arrays, *J. Atmos. Sci.*, *70*, 3157–3179.
Johnson, R. H., and X. Lin (1997), Episodic trade wind regimes over the western Pacific warm pool, *J. Atmos. Sci.*, *54*, 2020–2034.
Johnson, R. H., P. E. Ciesielski, J. H. Ruppert Jr., and M. Katsumata (2015), Sounding-based thermodynamic budgets for DYNAMO, *J. Atmos. Sci.*, *70*, 598–622.
Kerns, B. W., and S. S. Chen (2014), Equatorial dry air intrusion and related synoptic variability in MJO initiation during DYNAMO, *Mon. Weather Rev.*, *142*, 1326–1343.
Kiladis, G. N., K. H. Straub, and P. T. Haertel (2005), Zonal and vertical structure of the Madden–Julian Oscillation, *J. Atmos. Sci.*, *62*, 2790–2809.
Kim, D., A. H. Sobel, E. D. Maloney, D. M. W. Frierson, and I.-S. Kang (2011), A systematic relationship between intraseasonal variability and mean state bias in AGCM simulations, *J. Clim.*, *24*, 5506–5520.
Kim, D., M. S. Ahn, I. S. Kang, and A. D. Del Genio (2015), Role of longwave cloud–radiation feedback in the simulation of the Madden–Julian Oscillation, *J. Clim.*, *28*, 6979–6994.
Kim, J., D. E. Waliser, G. Cesana, X. Jiang, T. L'Ecuyer, and J. M. Neena (2017), Cloud and radiative heating profiles associated with the boreal summer intraseasonal oscillation, *J. Clim.*, in press.
Lappen, C.-L., and C. Schumacher (2014), The role of tilted heating in the evolution of the MJO, *J. Geophys. Res. Atmos.*, *119*, 2966–2989, doi:10.1002/2013JD020638.
Lee, M.-I., I.-S. Kang, J.-K. Kim, and B. E. Mapes (2001), Influence of cloud-radiation interaction on simulating tropical intra-seasonal oscillation with an atmosphere general circulation model, *J. Geophys. Res.*, *106*, 14,291–14,233.
Lin, J.-L., and B. E. Mapes (2004), Radiation budget of the tropical intraseasonal oscillation, *J. Atmos. Sci.*, *61*, 2050–2062.
Lin, J.-L., B. E. Mapes, M. Zhang, and M. Newman (2004), Stratiform precipitation, vertical heating profiles, and the Madden-Julian Oscillation, *J. Atmos. Sci.*, *61*, 296–309.
Lin, X., and R. H. Johnson (1996), Heating, moistening, and rainfall over the western Pacific warm pool during TOGA COARE, *J. Atmos. Sci.*, *53*(22), 3367–3383.

Ma, D., and Z. Kuang (2011), Modulation of radiative heating by the Madden-Julian Oscillation and convectively coupled Kelvin waves as observed by CloudSat, *Geophys. Res. Let.*, *38*, L21813, doi:10.1029/2011GL049734.
Madden, R. A., and P. R. Julian (1972), Description of global-scale circulation cells in the Tropics with a 40–50 day period, *J. Atmos. Sci.*, *29*, 1109–1123.
Mapes, B., S. Tulich, J. Lin, and P. Zuidema (2006), The mesoscale convection life cycle: Building block or prototype for large-scale tropical waves?, *Dyn. Atmos. Oceans*, *42*, 3–29.
Mather, J. H., S. A. McFarlane, M. A. Miller, and K. L. Johnson (2007), Cloud properties and associated heating rates in the tropical western Pacific, *J. Geophys. Res.*, *112*, D05201, doi:10.1029/2006JD007555.
Nitta, T., and S. Esbensen (1974), Heat and moisture budget analyses using BOMEX data, *Mon. Weather Rev.*, *102*, 17–28.
Petch, J. D., X. Waliser, P. X. Jiang, and S. Woolnough (2011), A global model inter-comparison of the physical processes associated the MJO, *GEWEX News*, *21*(3), 3–5.
Powell, S. W. (2016), Updraft buoyancy within and moistening by cumulonimbi prior to MJO convective onset in a regional model, *J. Atmos. Sci.*, *73*, 2913–2934.
Powell, S. W., and R. A. Houze (2015), The effect of dry large-scale vertical motions on initial MJO convective onset, *J. Geophys. Res. Atmos.*, *120*, 4783–4805, doi:10.1002/2014JD022961.
Powell, S. W., R. A. Houze Jr., and S. R. Brodzik (2016), Rainfall-type categorization of radar echoes using polar coordinate reflectivity data, *J. Atmos. Oceanic Technol.*, *33*, 523–538.
Raymond, D. J. (2001), A new model of the Madden–Julian Oscillation, *J. Atmos. Sci.*, *58*, 2807–2819.
Rienecker, M. M., et al. (2011), MERRA: NASA's Modern-Era Retrospective analysis for Research and Applications, *J. Clim.*, *24*, 3624–3648.
Ruppert, J. H., Jr., and R. H. Johnson (2015), Diurnally modulated cumulus moistening in the preonset stage of the Madden–Julian Oscillation during DYNAMO, *J. Atmos. Sci.*, *72*, 1622–1647.
Schubert, W. H., and M. T. Masarik (2006), Potential vorticity aspects of the MJO, *Dyn. Atmos. Oceans*, *42*, 127–151.
Schumacher, C., R. A. Houze Jr., and I. Kraucunas (2004), The tropical dynamical response to latent heating estimates derived from the TRMM precipitation radar, *J. Atmos. Sci.*, *61*, 1341–1358.
Sobel, A., and E. D. Maloney (2012), An idealized semi-empirical framework for the Madden–Julian Oscillation, *J. Atmos. Sci.*, *69*, 1691–1705.
Sobel, A., and E. D. Maloney (2013), Moisture modes and the eastward propagation of the MJO, *J. Atmos. Sci.*, *70*, 187–192.
Sobel, A., S. Wang, and D. Kim (2014), Moist static energy budget of the MJO during DYNAMO, *J. Atmos. Sci.*, *71*, 4276–4291.
Steiner, M., R. A. Houze Jr., and S. E. Yuter (1995), Climatological characterization of three-dimensional storm structure from operational radar and rain gauge data, *J. Appl. Meteorol.*, *34*, 1978–2007.
Stephens, G. L., M. J. Webb, P. J. Minnett, P. H. Daum, L. Kleinman, I. Wittmeyer, and D. A. Randall (1994), Observations of the Earth's radiation budget in relation to atmospheric hydrology. 4: Atmospheric column radiative cooling over the world's oceans, *J. Geophys. Res.*, *99*, 18,585–18,604, doi:10.1029/94JD01151.
Virts, K. S., and J. M. Wallace (2014), Observations of temperature, wind, cirrus, and trace gases in the tropical tropopause transition layer during the MJO, *J. Atmos. Sci.*, *71*, 1143–1157.
Wang, B., and F. Liu (2011), A model for scale interaction in the Madden-Julian Oscillation, *J. Atmos. Sci.*, *68*, 2524–2536.
Wang, S., and A. H. Sobel (2012), Impact of imposed drying on deep convection in a cloud-resolving model, *J. Geophys. Res.*, *117*, D02112, doi:10.1029/2011JD016847.
Webster, P. J., and G. L. Stephens (1980), Tropical upper-tropospheric extended clouds: Inferences from winter MONEX, *J. Atmos. Sci.*, *37*, 1521–1541.
Wielicki, B. A., B. R. Barkstrom, E. F. Harrison, R. B. Lee III, G. L. Smith, and J. E. Cooper (1996), Clouds and the Earth's Radiant Energy System (CERES): An Earth Observing System experiment, *Bull. Am. Meteorol. Soc.*, *77*, 853–868.
Wilks, D. E. (1995), *Statistical Methods in Atmospheric Science*, pp. 465, Academic Press, San Diego, Calif.
Wing, A. A., and K. A. Emanuel (2014), Physical mechanisms controlling self-aggregation of convection in idealized numerical modeling simulations, *J. Adv. Model Earth Syst.*, *6*, 59–73.
Wolding, B. O., E. D. Maloney, and M. Branson (2016), Vertically resolved weak temperature gradient analysis of the Madden-Julian Oscillation in SP-CESM, *J. Adv. Model Earth Syst.*, *8*, 1586–1619, doi:10.1002/2016MS000724.
Xie, S., R. T. Cederwall, and M. Zhang (2004), Developing long-term single-column model/cloud system-resolving model forcing data using numerical weather prediction products constrained by surface and top of the atmosphere observations, *J. Geophys. Res.*, *109*, D01104, doi:10.1029/2003JD004045.
Xu, W., and S. A. Rutledge (2014), Convective characteristics of the Madden–Julian oscillation over the central Indian Ocean observed by shipborne radar during DYNAMO, *J. Atmos. Sci.*, *71*, 2859–2877.
Xu, W., and S. A. Rutledge (2016), Time scales of shallow-to-deep convective transition associated with the onset of the Madden-Julian oscillation, *Geophys. Res. Lett.*, *43*, 2880–2888, doi:10.1002/2016GL068269.
Xu, W., S. A. Rutledge, C. Schumacher, and M. Katsumata (2015), Evolution, properties, and spatial variability of MJO convection near and off the equator during DYNAMO, *J. Atmos. Sci.*, *72*, 4126–4147.
Yanai, M., and R. H. Johnson (1993), Impacts of cumulus convection on thermodynamic fields, in *The Representation of Cumulus Convection in Numerical Models of the Atmosphere, Meteorol. Monogr.*, vol. 46, pp. 39–62, Am. Meteorol. Soc., Boston, Mass.
Yanai, M., S. Esbensen, and J.-H. Chu (1973), Determination of bulk properties of tropical cloud clusters from large-scale heat and moisture budgets, *J. Atmos. Sci.*, *30*, 611–627.
Yanai, M., B. Chen, and W.-W. Tung (2000), The Madden–Julian Oscillation observed during the TOGA COARE IOP: Global view, *J. Atmos. Sci.*, *57*, 2374–2396.
Yoneyama, K., C. Zhang, and C. N. Long (2013), Tracking pulses of the Madden–Julian Oscillation, *Bull. Am. Meteorol. Soc.*, *94*, 1871–1891.
Yu, J. Y., C. Chou, and J. D. Neelin (1998), Estimating the gross moist stability of the tropical atmosphere, *J. Atmos. Sci.*, *55*, 1354–1372.
Zhang, C. (2013), The Madden–Julian Oscillation: Bridging weather and climate, *Bull. Am. Meteorol. Soc.*, *94*, 1849–1870.
Zhang, C., J. Gottschalck, E. D. Maloney, M. W. Moncrieff, F. Vitart, D. E. Waliser, B. Wang, and M. C. Wheeler (2013), Cracking the MJO nut, *Geophys. Res. Lett.*, *40*, 1223–1230, doi:10.1002/grl.50244.
Zhang, M. H., and J. L. Lin (1997), Constrained variational analysis of sounding data based on column-integrated budgets of mass, heat, moisture, and momentum: Approach and application to ARM measurements, *J. Atmos. Sci.*, *54*, 1503–1524.
Zhang, M. H., J. L. Lin, R. T. Cederwall, J. J. Yio, and S. C. Xie (2001), Objective analysis of ARM IOP data: Method and sensitivity, *Mon. Weather Rev.*, *129*, 295–311.